Analysis of the grain size evolution for ferrite formation in Fe-C-Mn steels using a 3D model under a mixed-mode interface condition

Fang, H.; Mecozzi, M. G.; Brück, E.; van der Zwaag, S.; van Dijk, N.H.

Analysis of the Grain Size Evolution for Ferrite Formation in Fe-C-Mn Steels Using a 3D Model Under a Mixed-Mode Interface Condition

H. FANG, M.G. MECOZZI, E. BRÜCK, S. VAN DER ZWAAG, and N.H. VAN DIJK

A 3D model has been developed to predict the average ferrite grain size and grain size distribution for an austenite-to-ferrite phase transformation during continuous cooling of an Fe-C-Mn steel. Using a Voronoi construction to represent the austenite grains, the ferrite is assumed to nucleate at the grain corners and to grow as spheres. Classical nucleation theory is used to estimate the density of ferrite nuclei. By assuming a negligible partition of manganese, the moving ferrite–austenite interface is treated with a mixed-mode model in which the soft impingement of the carbon diffusion fields is considered. The ferrite volume fraction, the average ferrite grain size, and the ferrite grain size distribution are derived as a function of temperature. The results of the present model are compared with those of a published phase-field model simulating the ferritic microstructure evolution during linear cooling of an Fe-0.10C-0.49Mn (wt pct) steel. It turns out that the present model can adequately reproduce the phase-field modeling results as well as the experimental dilatometry data. The model presented here provides a versatile tool to analyze the evolution of the ferrite grain size distribution at low computational costs.

I. INTRODUCTION

FE-C-MN steels hold and retain an important position in high-quality construction and automotive steels, and therefore, their transformation behavior receives a lot of attention in academia and industry.[1–6] Their mechanical properties, which are controlled by their microstructure, can be tuned relatively easily by thermomechanical processing. Ferrite is the first transformation product that forms during cooling as a result of austenite decomposition. Therefore understanding the decomposition of austenite (γ) into ferrite (α) during cooling is of central importance for predicting the development of the microstructure during thermomechanical processes. This is the reason why the austenite-to-ferrite transformation has been studied extensively, both experimentally and theoretically.[7–12] A recent detailed overview on all physical aspects of this transformation is presented by Gouné and coworkers.[13]

During the austenite-to-ferrite phase transformation, the volume fraction and the grain size distribution of the ferrite fraction play a key role in the development of the ferritic microstructure. Traditional *in situ* experimental techniques, like dilatometry, only determine the total fraction transformed, but yield no information on the evolution of the ferrite grain size. Such complementary information can however be obtained by micro-beam X-ray diffraction[14,15] and three-dimensional neutron depolarization.[16,17] These *in situ* techniques provide a more detailed view on the microstructure development, but cannot monitor the evolution in chemical composition profile. The aim of this work is to establish a concise 3D model to achieve a comprehensive description of the austenite-to-ferrite transformation and to obtain quantitative information on the ferrite volume fraction, grain size distribution, and carbon diffusion profiles in the austenite at relatively low computational costs.

In the following, we will first define the 3D austenite-to-ferrite transformation model. This model is inspired by the topological transformation models established by Te Velthuis and coworkers[18] and Offerman and coworkers.[19] The predictions of our new

H. FANG is with the Fundamental Aspects of Materials and Energy group, Faculty of Applied Sciences, Delft University of Technology, Mekelweg 15, 2629 JB Delft, The Netherlands and also with the Novel Aerospace Materials group, Faculty of Aerospace Engineering, Delft University of Technology, Kluyverweg 1, 2629 HS Delft, The Netherlands. Contact e-mail: H.Fang@tudelft.nl M.G. MECOZZI is with the Department of Materials Science and Engineering, Delft University of Technology, Mekelweg 2, 2628 CD Delft, The Netherlands. E. BRÜCK and N.H. VAN DIJK are with the Fundamental Aspects of Materials and Energy group, Faculty of Applied Sciences, Delft University of Technology. S. VAN DER ZWAAG is with the Novel Aerospace Materials group, Faculty of Aerospace Engineering, Delft University of Technology.
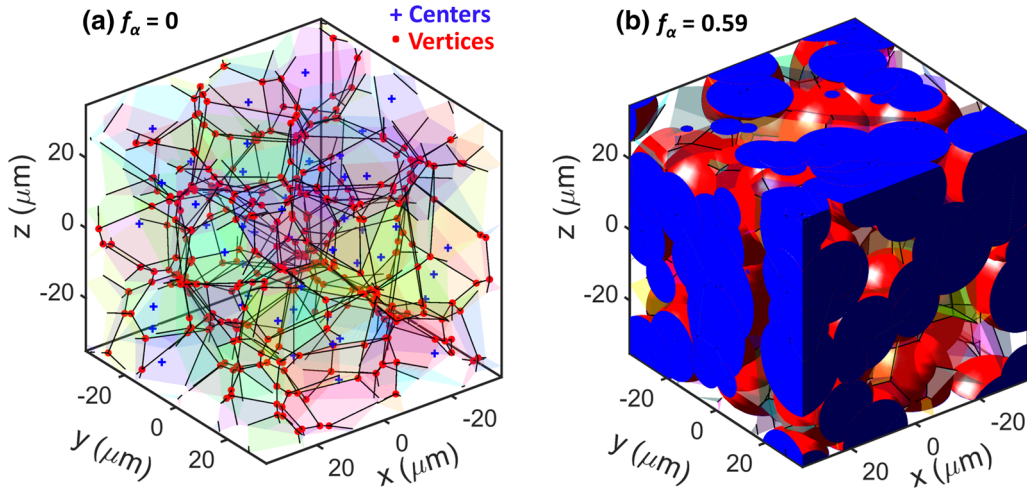Manuscript submitted April 4, 2017.

Fig. 1—(a) Initial austenite structure represented by Voronoi cells and (b) a 3D view of the transformed structure with a ferrite volume fraction of $f_\alpha = 0.59$ in a cubic box with a length of $L_b = 70$ μm (spherical ferrites surface shown in red and their cut-off plane on the edge of the box is shown in blue) (Color figure online).

transformation model are presented for an Fe-0.10C-0.49Mn (wt pct) steel cooled at modest constant cooling rates starting from a single-phase austenite. These results are then compared to the previously presented predictions from a computationally more demanding phase-field model,[20] as well as the experimental results obtained from dilatometry. Special attention is given to the predicted ferrite grain size distribution as a function of the assumed nucleation behavior, as advanced experimental methods, such as neutron depolarization, emerge which will enable the *in situ* experimental determination of this grain size distribution during linear cooling.

II. MODEL DESCRIPTION

In the following, we present an analytical model for the ferritic microstructure evolution. The 3D microstructure model assumes that the new ferrite phase nucleates at Voronoi vertices (grain corners) and grows isotropically (as a sphere). The number of ferrite nuclei formed is calculated using classical nucleation theory (CNT).[21–23] The moving austenite–ferrite interface is treated as progressing under mixed-mode[24] conditions. Analytical expressions for the carbon concentration at the interface and far away from the interface are derived for non-overlapping and overlapping of diffusion fields (soft impingement). As the transformation proceeds, the growing ferrite grains may also get in contact with other ferrite grains (hard impingement). As local contact between neighboring ferrite grains does not exclude further growth of the ferrite by the motion of the non-pinned part of the interface, the further growth after the onset of hard impingement is also modeled.

A. Starting Structure

The parent structure is fully austenite with a given number density ρ_γ of austenite grains represented in a cubic box of length L_b in which periodic boundary conditions are applied. The average austenite grain size corresponds to $\bar{d}_\gamma = (6/\pi\rho_\gamma)^{1/3}$. The austenite grain centers are generated randomly with a minimum distance d_{min} to control the grain size distribution. Voronoi cells are subsequently constructed to represent the austenite grains. The vertices of the Voronoi cells are assumed to be the potential nucleation sites for the forming ferrite phase as its nucleation is found to be predominantly taking place at grain corners.[25] In the present work, the Voronoi cells are constructed by using the Multi-Parametric Toolbox[26] in the Matlab environment. An initial austenite structure is shown in Figure 1(a) and a 3D view of the same domain after partial austenite transformation to a ferrite fraction of 0.59 is shown in Figure 1(b).

B. Ferrite Nucleation

The reduction in Gibbs free energy for the new ferritic phase with respect to the parent austenite phase provides the driving force for the austenite-to-ferrite transformation. At the same time, the creation of new interfaces requires a consumption of energy. The competition between these two effects results in a change in Gibbs free energy ΔG that depends on the cluster size n. At a critical cluster size n^*, the change in Gibbs free energy shows a maximum value ΔG^*, which is the activation barrier for nucleation. When this activation barrier ΔG^* is large compared to the thermal energy $k_B T$ (where k_B is Boltzmann's constant and T the temperature in kelvin), then the Classical Nucleation Theory (CNT) describes the nucleation kinetics in polycrystalline materials.[27,28] Recently, Sharma and coworkers[29] estimated that $\Delta G^* \approx 3$ to $6 k_B T$ for the nucleation of austenite in ferrite. Similar small values are observed for the nucleation of ferrite in austenite.[27] According to the CNT, the steady-state nucleation rate per unit of volume $\dot{N}$ can be expressed as[27]

$$\dot{N} \propto Z N_p \beta^* \exp\left(-\frac{\Delta G^*}{k_B T}\right), \qquad [1]$$

where Z is the Zeldovich factor; N_p the number density of potential nucleation sites; β^* the frequency factor; k_B the Boltzmann constant; and T the temperature in kelvin. The Zeldovich factor is nearly constant ($Z \approx 0.05$) and accounts for the width of the nucleation barrier on the effective number of clusters that become supercritical. N_p is decreasing during the austenite-to-ferrite transformation due to the consumption of potential nucleation sites by (i) the nucleation itself and (ii) by ferrite growth. As the density of potential nucleation sites is relatively high, N_p is assumed to be proportional to the untransformed volume fraction. The frequency factor can be expressed as $\beta^* \propto v \exp[-Q_D/(k_B T)]$, where Q_D is the energy barrier for diffusion; $v \approx k_B T/h$ is the attempt frequency; and h is Planck's constant. The energy barrier for nucleation ΔG^* is given by

$$\Delta G^* = \frac{\Psi}{(\Delta G_V - \Delta G_S)^2}, \qquad [2]$$

where Ψ is a constant that comprises all the information of the shape of the critical nucleus and interfacial energies between the nucleus and the surrounding parent grains. A value of $\Psi \approx 5 \times 10^{-8}$ J^3 m^{-6} [14] is used in the present work. ΔG_V is the difference in Gibbs free energy per unit volume between ferrite and austenite, which is calculated with Thermo-Calc under para-equilibrium conditions. ΔG_S is the misfit strain energy due to the difference in volume between ferrite and austenite and is estimated to be $\Delta G_S \approx 1 \times 10^7$ J m^{-3}.[30] In the present work, ΔG_S is assumed to be 0.7×10^7 J m^{-3} to adjust the starting nucleation temperature. The nucleation rate can thus be written as

$$\dot{N} = A Z N_0 (1 - f_\alpha)\left(\frac{k_B T}{h}\right)\exp\left(-\frac{Q_D}{k_B T}\right)$$
$$\times \exp\left(-\frac{\Psi}{k_B T(\Delta G_V(T) - \Delta G_S)^2}\right), \qquad [3]$$

where A is a constant and N_0 represents the number of potential nucleation sites at the austenite grain corners at the start of the transformation.

C. Ferrite Growth

After nucleation the ferrite grains are assumed to grow isotropically, hence to grow as spheres. Using the mixed-mode concept,[24] the interface velocity v is proportional to product of the local chemical driving force ΔG and the interface mobility M

$$v = M\Delta G. \qquad [4]$$

The interface mobility M is temperature dependent:

$$M = M_0 \exp\left(-\frac{Q_M}{RT}\right), \qquad [5]$$

where M_0 is a constant and $Q_M = 140$ kJ mol^{-1}[31] is the activation energy for atomic motion. It should be noted that M_0 in Eq. [5] corresponds to an effective interface mobility, which accounts for the lattice reconstruction, solute drag effect due to substitutional alloying elements,[32] pinning effects of precipitates at the grain boundary,[33] and the direction of the transformation.[34]

The local driving force ΔG depends on the solute concentrations at the interface. In this model, it is assumed that the carbon concentration in the ferrite is homogeneous and equal to the equilibrium value $C_{eq}^{\alpha\gamma}$. Therefore, ΔG can be formulated as

$$\Delta G = \chi\left(C_{eq}^{\gamma\alpha} - C^\gamma\right), \qquad [6]$$

where χ is a proportionality factor (that can be calculated with Thermo-Calc); $C_{eq}^{\gamma\alpha}$ is the equilibrium carbon concentration in austenite; and C^γ is the carbon concentration at the interface at the austenite side. To calculate the interface velocity v, the value of C^γ is required. For each ferrite grain, the growth velocity is expected to be different at each time step as the time since nucleation and the distance to neighboring ferrite grain differs. In the following the treatment used to calculate the interface velocity at distinctly different stages of the transformation is discussed.

1. Non-overlapping of diffusion fields

As illustrated in Figure 2(a), at an early stage of ferrite growth the diffusion fields surrounding these ferrite grains do not overlap. In this case the carbon concentration far away from the γ/α interface (C_∞) equals the nominal concentration (C_0): $C_\infty = C_0$. In such a condition, the carbon concentration profile surrounding the ferrite grains, $C(r)$, can be approximated by a second-order polynomial,[35] where the carbon concentration as a function of the distance r from the interface ($r = 0$ at the γ/α interface) is given by

$$C(r) = C_0 + (C^\gamma - C_0)\left(1 - \frac{r}{L}\right)^2 \quad (0 \leq r \leq L), \quad [7]$$

where L is the diffusion length. This concentration profile fulfills the following boundary conditions:

$$C(r = 0) = C^\gamma \qquad [8]$$

$$C(r = L) = C_0. \qquad [9]$$

There is no concentration gradient at the position of diffusion length L:

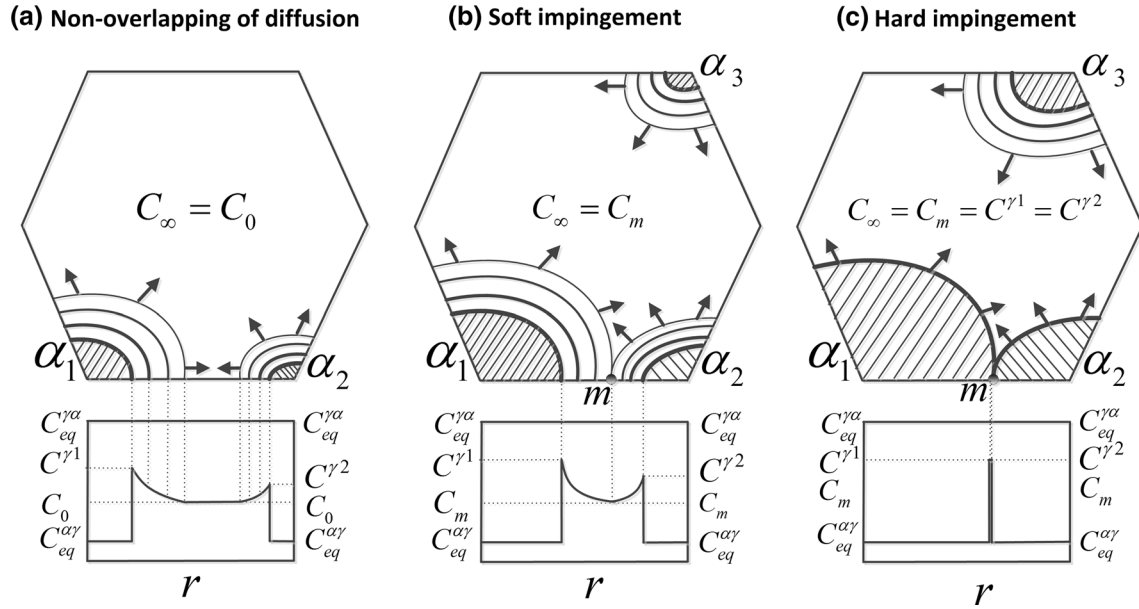$$\left.\left(\frac{\partial C}{\partial r}\right)\right|_{r=L} = 0, \qquad [10]$$

(a) Non-overlapping of diffusion   **(b) Soft impingement**   **(c) Hard impingement**

Fig. 2—Sketch of the development of carbon diffusion profiles during the growth of the α phase into the γ phase in the (*a*) early stage without overlap of diffusion fields; (*b*) middle stage where diffusion fields starts to overlap (soft impingement); and (*c*) late stage where neighboring α grains start to show direct contact with each other (hard impingement). For clarity, these stages in ferrite growth are only shown within one γ grain. Arrows indicate the growth direction of the α phase. The shaded parts are the α phase and the surrounding curves indicate the diffusion fields with a gradient in carbon concentration.

Considering a ferrite grain radius of R_α, the mass conservation of carbon can be expressed as

$$\int_0^{R_\alpha}\left(C_0 - C_{\text{eq}}^{\alpha\gamma}\right)4\pi r^2 \mathrm{d}r = \int_0^L (C(r) - C_0)4\pi(r + R_\alpha)^2\mathrm{d}r.$$
[11]

Combining Eqs. [7] through [11] results in

$$\left(C_0 - C_{\text{eq}}^{\alpha\gamma}\right)V_\alpha = 4\pi \int_0^L (C(r) - C_0)(r + R_\alpha)r^2\mathrm{d}r$$
$$= -\frac{4\pi(C_0 - C^\gamma)\left(L^3 + 5L^2 R_\alpha + 10LR_\alpha^2\right)}{30},$$
[12]

where $V_\alpha = 4\pi R_\alpha^3/3$ is the ferrite grain volume. During the ferrite growth there is no carbon accumulation at the interface. Then, the following equation can be derived:

$$v\left(C^\gamma - C_{\text{eq}}^{\alpha\gamma}\right) = M\chi\left(C_{\text{eq}}^{\gamma\alpha} - C^\gamma\right)\left(C^\gamma - C_{\text{eq}}^{\alpha\gamma}\right) = -D\left(\frac{\partial C}{\partial r}\right)\Big|_{r=0},$$
[13]

where D the carbon diffusivity in austenite calculated according to Reference 36. The mixed-mode nature of the transformation, quantified by the mode parameter $S = (C^{\gamma\alpha} - C^\gamma)/(C^{\gamma\alpha} - C_0)$, is controlled by parameter $z = (D/M\chi)(A_\alpha/V_\alpha)$, where A_α is the interfacial area of the growing ferrite grain.[37] The extreme cases correspond to (i) diffusion control for $z = 0$ and (ii) interface control for $z = \infty$.[24] Taking the derivative of $C(r)$ at $r = 0$ from Eq. [7] and inserting it into Eq. [13] results in

$$\frac{2D}{LM\chi}(C_0 - C^\gamma) = \left(C_{\text{eq}}^{\gamma\alpha} - C^\gamma\right)\left(C_{\text{eq}}^{\alpha\gamma} - C^\gamma\right),$$
[14]

with an interface velocity $v = 2D/L$. One can now derive the interfacial carbon concentration C^γ and the diffusion length L by solving the set of Eqs. [12] and [14]. Theoretically there is more than one solution for C^γ and L for this set of functions. However, one can only find one unique real solution for C^γ with $C_0 \leq C^\gamma \leq C_{\text{eq}}^{\gamma\alpha}$ and $L > 0$.

The condition of non-overlapping carbon diffusion fields around two neighboring growing ferrite grains is then given by

$$R_{\alpha,i} + L_i + R_{\alpha,j} + L_j < r_{ij} \quad (i \neq j),$$
[15]

where i and j refer to specific ferrite grains; r_{ij} is the distance between ferrite grain i and j; and R_α and L are the radius and diffusion length, respectively. Figure 2(a) schematically illustrates the case in which the carbon diffusion profiles around two neighboring ferrite grains do not overlap and the growth of one grain does not influence the growth of the other.

2. Soft impingement

With the progression of the austenite-to-ferrite transformation, the diffusion field surrounding a growing ferrite grain may start to overlap with that of a neighboring one. In Figure 2(b), the diffusion profile around grain 1 starts to intersect the profile around grain 2 at point m. This happens when the following condition is fulfilled:

$$R_{\alpha,i} + L_i + R_{\alpha,j} + L_j = r_{ij} \quad (i \neq j).$$
[16]

Assuming that the carbon outside the soft impingement region can diffuse fast enough in the matrix of the austenite grain to let the bulk carbon concentration be homogenous, we have $C_\infty = C_m$, where C_m is the carbon concentration at the soft impingement point. At this stage the carbon concentration profile can be written as

$$C(r) = C_m + (C^\gamma - C_m)\left(1 - \frac{r}{L}\right)^2 \quad (0 \le r \le L), \quad [17]$$

which fulfills the following conditions:

$$C(r = 0) = C^\gamma \qquad [18]$$

$$C(r = L) = C_m \qquad [19]$$

$$\left.\frac{\partial C}{\partial r}\right|_{r=L} = 0. \qquad [20]$$

Similar to the non-overlapping stage, mass conservation of carbon results in

$$\left(C_0 - C_{eq}^{\alpha\gamma}\right)V_\alpha = 4\pi \int_0^L \left[(C_m - C_0) + (C^\gamma - C_m)\left(1 - \frac{r}{L}\right)^2\right](r + R_\alpha)^2 \mathrm{d}r$$
$$= \frac{2\pi L\left(9L^2 C_m - 10L^2 C_0 + L^2 C^\gamma + 20R_\alpha^2 C_m - 30R_\alpha^2 C_0 + 10R_\alpha^2 C^\gamma + 25LR_\alpha C_m - 30LR_\alpha C_0 + 5LR_\alpha C^\gamma\right)}{15}. \qquad [21]$$

Equation [13] also applies for this stage due to the absence of carbon accumulation at the interface:

$$\frac{2D}{\chi ML}(C_m - C^\gamma) = \left(C_{eq}^{\gamma\alpha} - C^\gamma\right)\left(C_{eq}^{\alpha\gamma} - C^\gamma\right). \qquad [22]$$

During the ferrite grain growth, the diffusion field is first treated without soft impingement to derive the diffusion length L. When the derived diffusion length fulfills Eq. [16] for a specific ferrite grain, soft impingement happens at that moment and one could regard this diffusion length L as the maximum distance that carbon can diffuse for that grain. By combining Eqs. [21] and [22], one can derive the unique solution for C^γ and C_m. In Figure 2(b), the diffusion fields for ferrite grains 1 and 2 intersect at point m. This means that the diffusion length for grain 1 cannot extend beyond point m (and similarly for grain 2). Soft impingement further results in $C_\infty = C_m$, which slows down the growth of other ferrite grains nucleated at other sites of the same austenite grain although they may not show soft impingement with any grain (see for example grain 3 in Figure 2(b)).

3. *Hard impingement*
After soft impingement has set in, further growth of the ferrite grains reduces the diffusion length until the

grains are in physical local contact with each other, that means

$$R_{\alpha,i} + R_{\alpha,j} = r_{ij} \quad (i \ne j). \qquad [23]$$

At this stage, due to the hard impingement, the diffusion length of the ferrite grains locally decreases to zero and the carbon concentration in the austenite matrix becomes homogeneous and equal to the interfacial concentration (see Figure 2(c)). Then the remaining average carbon concentration in the remaining austenite fraction of the original austenite grain can be calculated with

$$C_\infty = \frac{C_0 - C_{eq}^{\alpha\gamma} f_\alpha^\gamma}{1 - f_\alpha^\gamma}, \qquad [24]$$

where f_α^γ is the volume fraction of ferrite in a specific austenite grain. It is assumed that available angular space for ferrite grain growth is equally distributed over the number of surrounding austenite grains. After correcting the intersection volume of ferrite spheres, f_α^γ for a specific austenite grain can be derived by

$$f_\alpha^\gamma = \frac{1}{V_{\gamma 0}} \sum_{i=1}^n \frac{V_{\alpha,i}}{n_i}, \qquad [25]$$

where $V_{\alpha,i}$ is the actual ferrite volume after subtracting the volume intersection; n_i is the number of austenite grains surrounding ferrite α_i; and $V_{\gamma 0}$ is the initial volume of the austenite grain. The method to correct the volume for two and three impinging spheres is explained in References 18 and 38. As the transformation proceeds, it is possible that a grain may impinge with three (or more) ferrite grains at a later stage. When this happens, it becomes much more complex to analytically calculate the intersecting volume, resulting in an extensive increase in computational costs. When a ferrite grain impinges with more than two other ferrite grains, we derive its corrected volume $V_{\alpha,i}$ with the following approach[39]:

$$V_{\alpha,i} = V_{\text{local},i} \tanh\left(\frac{V_{\alpha,i}^e}{V_{\text{local},i}}\right), \qquad [26]$$

where $V_{\text{local},i}$ is the combined ferrite grain volume ($V_{\alpha,i}$) with the available untransformed surrounding austenite grain volume, and $V_{\alpha,i}^e$ the extended volume of grain i

(before correcting for hard impingement). With this method the volume of each ferrite grain can be corrected explicitly for the impingement of four or more ferrite grains.

D. Computational Procedure

The length of the cubic sample box is set as $L_b = 70~\mu m$ and the average austenite grain size is $\bar{d}_\gamma = 20~\mu m$ ($\rho_\gamma = 2.4 \times 10^{14}~m^{-3}$) with $d_{\min} = 12~\mu m$. This results in 82 austenite grains in the starting structure and 392 vertices of Voronoi cells as potential nucleation sites for the ferrite phase. For a specific Fe-C-Mn steel, the para-equilibrium A_3 temperature is calculated with Thermo-Calc. The phase boundary lines of $(\alpha + \gamma)/\gamma$ and $\alpha/(\alpha + \gamma)$ are also calculated and fitted in the temperature range of interest with a second-order polynomial to define the equilibrium carbon concentrations $C_{eq}^{\alpha\gamma}$ and $C_{eq}^{\gamma\alpha}$ and the equilibrium ferrite volume fraction:

$$f_\alpha^{eq} = \frac{C_{eq}^{\gamma\alpha} - C_0}{C_{eq}^{\gamma\alpha} - C_{eq}^{\alpha\gamma}}. \qquad [27]$$

The difference in Gibbs free energy per unit of volume between the ferrite phase and austenite phase ΔG_V is calculated as described by Mecozzi and coworkers.[20] The proportionality factor χ is first calculated with Thermo-Calc (under para-equilibrium conditions) and then fitted as a function of temperature. The value for the pre-factor of the interface mobility expression M_0 is pre-defined to match the phase-field simulations and is close to the experimental value determined by Krielaart and coworkers.[31] It should be noted that there are many values of M_0 reported in literature. Hillert and Höglund[40] reviewed these values and confirmed that the value reported in Reference 31 was consistent with the experimental measurements for Fe-X (X = Mn, Co or Ni) alloys containing low amounts of carbon. In a recent publication by Zhu and coworkers,[41] accurate values for the intrinsic mobility of the austenite–ferrite interface for interstitial-free Fe-X alloys are presented.

An iterative process with a time step Δt is adopted to predict the evolution of the ferrite transformation. At the start of the transformation the initial parameters are $t = 0$, $T = A_3$, and $f_\alpha = 0$. The temperature T is then assumed to decrease at a constant cooling rate. For each time step, the number of nuclei is derived from CNT with the local driving force at each potential nucleation site. At each time step, new nuclei will attempt to form at the potential nucleation sites, provided that the distance to a nucleated ferrite grain is bigger than a preset distance d_{shield}, which is defined as a quarter of the average spacing between ferrite grains ($d_{shield} = \rho_\alpha^{-1/3}/4$). Moreover, new nuclei are assumed to be formed preferably at the site where the local driving force (based on the carbon concentration on that site) is most favorable for nucleation. This means that the nucleation process is influenced by the pre-formed nuclei in terms of both spatial correlation and carbon distribution. The interface velocity for each ferrite grain

is calculated by deriving the carbon concentration at the austenite/ferrite interface (C^γ) and in the bulk of austenite grain (C_∞), as discussed in Section II–C. As a result, the ferrite grain radius of grain i at time t is calculated from the previous interface position and velocity by

$$R_{\alpha,i}(t) = R_{\alpha,i}(t - \Delta t) + v_i(t - \Delta t)\Delta t. \qquad [28]$$

When this specific grain i starts to show hard impingement with other grains, an effective radius is derived from the ferrite grain volume corrected for the overlap volume V_i. After each time step, the microstructural characteristics including the ferrite volume fraction f_α; the effective ferrite grain radius $R_{\alpha,i}$; the average grain radius δ_s; and the standard deviation σ_p for the ferrite grain radius are calculated as follows:

$$f_\alpha = L_b^{-3} \sum_{i=1}^{N} V_{\alpha,i} \qquad [29]$$

$$R_{\alpha,i} = \left(3V_{\alpha,i}/4\pi\right)^{1/3} \qquad [30]$$

$$\delta_s = \left\langle R_{\alpha,i} \right\rangle \qquad [31]$$

$$\sigma_p = \left[\frac{1}{N-1} \sum_{i=1}^{N} \left(R_{\alpha,i} - \left\langle R_{\alpha,i} \right\rangle\right)^2 \right]^{\frac{1}{2}}. \qquad [32]$$

Furthermore, the interfacial and remote matrix carbon concentration, the diffusion length for each ferrite grain, and the chemical composition of the surrounding austenite grains are calculated after each time step. The iterative process continues until either the equilibrium ferrite fraction f_α^{eq} or the A_1^- temperature is reached.

The present model is employed to simulate the ferrite transformation in an Fe-0.10C-0.49Mn (wt pct) steel during continuous cooling. The steel composition and transformation conditions were chosen equal to those in a previous computational study using a 3D phase-field model[20,42] which used the MICRESS (MICrostructure Evolution Simulation Software) code developed by Steinbach and coworkers.[43,44] The A_3 and A_1^- temperature of this steel are calculated to be 1116 K and 984 K (843 °C and 711 °C), respectively. A comparison is made between the results of the present model and those of the phase-field simulations, where the nuclei were allowed to form over a nucleation temperature range, δT, with a constant nucleation rate. These phase-field simulations employed a simplified linear, fixed temperature interval nucleation model (SNM).

To allow a better comparison between the results of our model and those of the phase-field model, we adjusted the nucleation parameters in the classical nucleation theory (CNT) to achieve two types of nucleation kinetics: (i) the final nuclei number density is the same as obtained for the SNM; (ii) the onset nucleation rate is the same as obtained for the SNM.

The two different conditions are shown in Figure 3. The nucleation for the CNT starts at the same temperature as for the SNM. The simulation conditions are summarized in Table I. The goal of the simulations is to investigate the effect of the nucleation temperature range on the transformation kinetics, with an emphasis on the evolution of the ferrite grain size distribution.

III. RESULTS

A. *Comparison Between the Present Model and the Phase-Field Model*

The initial calculations of the transformation kinetics with the present model use exactly the same parameters for the simplified nucleation model as used in the
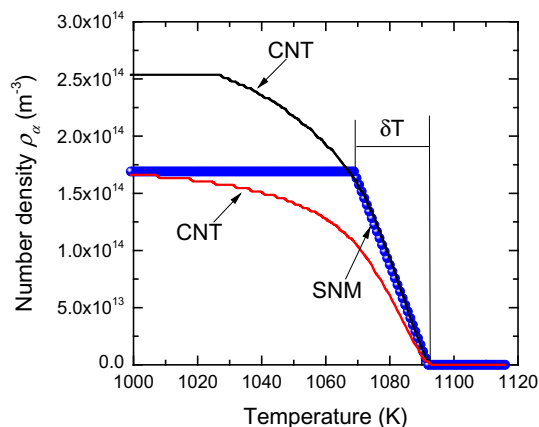

Fig. 3—Effect of the nucleation temperature range δT on the number density of ferrite grains ρ_α. The spheres show the data for the simple nucleation model (SNM), while solid curves represent the corresponding data for the classical nucleation theory (CNT) when (i) the final density of ferrite grains is equal (red line) or (ii) when the initial ferrite nucleation rate is equal (black line) (Color figure online).

reference phase-field model. Figure 4 shows the ferrite grain microstructure and ferrite grain size distribution at different transformation stages during cooling for $\delta T = 0$ and 24 K. For $\delta T = 0$ K, a total number of 58 nuclei form at the same time (site saturation), which results in a single ferrite grain size at $f_\alpha = 0.01$, while a small spread in grain size is present at $f_\alpha = 0.25$ due to hard impingement. Notably there are some ferrite grains that grow out of the edge of the cubic box so that they partially appear at different locations due to the periodic boundary conditions. For $\delta T = 24$ K, the ferrite nuclei continuously form in a temperature range of 24 K, which results in an increase of the spread in ferrite grain size distribution during the transformation. The ferrite grains that nucleate earlier grow to bigger sizes than the ones that nucleate later. This is reflected in the broad ferrite grain size distribution of Figure 4(g) originating from the spread in nucleation time. In the early growth stage, soft impingement hardly occurs and therefore the ferrite grain growth is not significantly influenced by other grains at this stage. In later stages, the size distribution becomes more irregular due to a progressive soft and hard impingement, as shown in Figures 4(d) and (h). The earlier formed ferrite grains with bigger grain sizes impinge with neighboring grains causing their growth to slow down, whereas the grains that nucleate later and have smaller sizes are still growing relatively fast without impediment. In Figure 4(h), a wide grain size distribution is observed in which all grain sizes up to 11 μm are present.

Figure 5(a) compares the kinetics of the austenite-to-ferrite transformation for different values of δT using the present model and the phase-field model. Both use the simplified nucleation model. The equilibrium ferrite fraction of Fe-0.10C-0.49Mn (wt pct) as calculated by the Thermo-Calc package under para-equilibrium condition is also added. In both models, increasing the nucleation temperature range delays the transformation kinetics; this is because more nuclei can form and grow to a larger size for a smaller δT at the same

Table I. Selected Simulation Parameters with the Cooling Rate $dT/dt = 0.4$ K s^{-1}, the Nuclei Density ρ_{max}, the Interface Mobility M_0, the Nucleation Temperature Range δT, and the Final Averaging Spacing of Ferrite Grains $\rho_{max}^{-1/3}$ for a Comparison with the Results from Previous Phase-Field Modeling.[20]

Model Trans.	Domain Size (μm^3)	Austenite Grains	ρ_{max} ($\times 10^{15}$ m^{-3})	$\rho_{max}^{-1/3}$ (μm)	Model Nucl.	M_0 ($\times 10^{-6}$ m^4 J^{-1} s^{-1})	δT (K)
Phase-field	$45 \times 45 \times 45$	12	0.17	18.0	SNM	0.24	0
							12
							24
						0.35	18
						0.38	24
Present model	$70 \times 70 \times 70$	82	0.17	18.0	SNM	0.24	0
							12
							24
						0.15	0
						0.26	18
						0.3	24
			0.17	18.0	CNT	0.3	24
			0.25	15.8		0.3	24

The results of the current transformation model are compared to those from the to the phase-field model. For the current model, two different nucleation models (SNM and CNT) are applied.
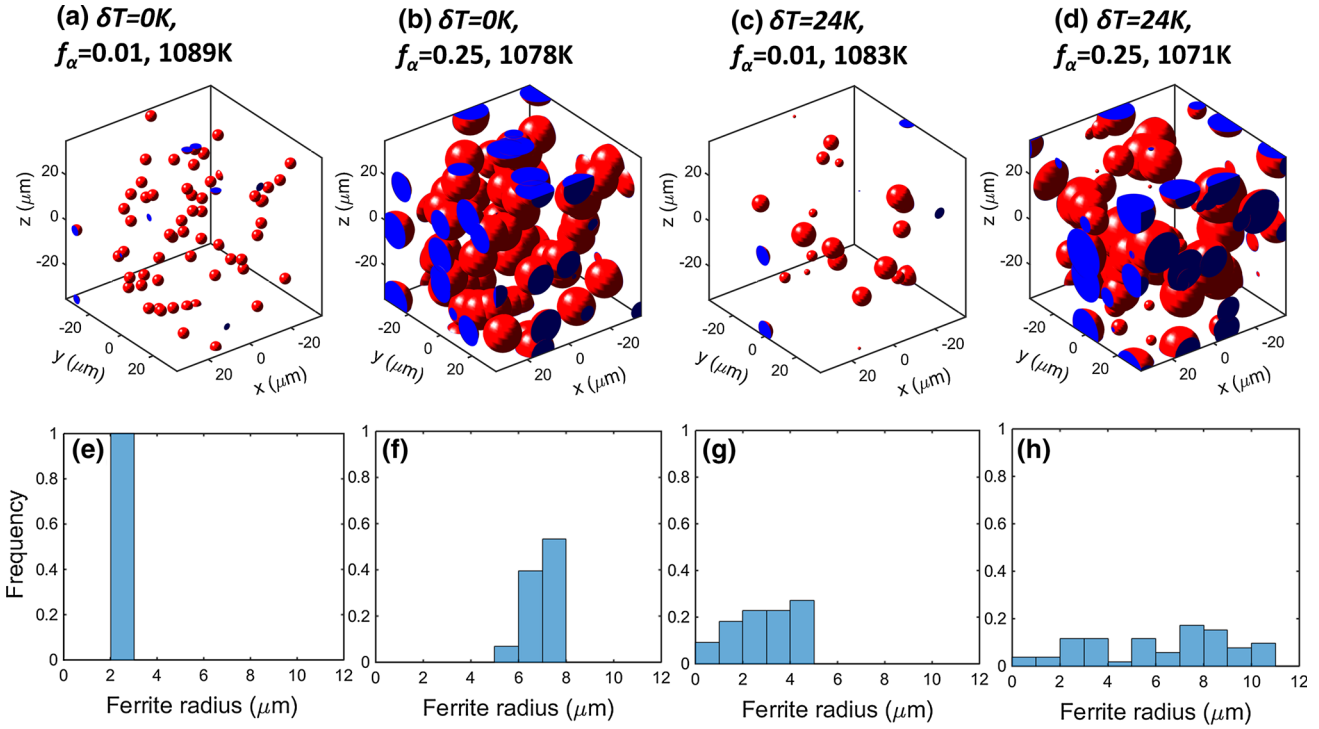
Fig. 4—Development of the formed ferrite grains for $\rho_0 = 0.17 \times 10^{15}$ m^{-3} and $M_0 = 0.24 \times 10^{-6}$ m^4 J^{-1} s^{-1} at a constant cooling rate of 0.4 K/s for (a) $\delta T = 0$ K and $f_\alpha = 0.01$; (b) $\delta T = 0$ K and $f_\alpha = 0.25$; (c) $\delta T = 24$ K and $f_\alpha = 0.01$; (d) $\delta T = 24$ K and $f_\alpha = 0.25$. Below the corresponding ferrite grain size distribution is shown (e) through (h). For clarity, the austenite structure is not shown.

transformation time (and corresponding temperature during continuous cooling). The total fraction transformed ultimately approaches the same equilibrium fraction, $f_\alpha \approx 0.7$. However, the present model predicts a faster kinetics than the phase-field model for simulations with the same δT. The kinetics of the phase-field simulation with $\delta T = 0$ K is in between the simulations of the present model with $\delta T = 12$ and 24 K. This difference cannot be caused by model inputs such as nucleation parameters, thermodynamic, and carbon diffusivity data, as these are effectively the same. Instead, the reason could be the difference in computational approach. The present model assumes isotropic growth, whilst the phase-field model allows different morphologies to form and takes into account the capillarity effect ($2\sigma_{\alpha\gamma}/R_\alpha$ in 3D, where $\sigma_{\alpha\gamma}$ is the α/γ interface energy), which consumes part of the chemical driving force during the growth of the ferrite. This capillarity effect, though decreases with increasing R_α, plays a non-negligible role, particularly in the early stage of the phase transformation, which slows down the ferrite growth in the phase-field simulation. However, the resulting geometrical differences between the present model and phase-field simulation are small as ferrite grains also grow more or less spherically in the phase-field simulations when $f_\alpha < 0.3$.[42]

Although a considerable difference is observed in the transformation kinetics for these two models, the average grain size δ_s and the standard deviation σ_p of the grain size distribution, show a comparable evolution as a function of f_α. The value of δ_s increases nearly at the same speed for both models in the intermediate

transformation stage ($0.2 < f_\alpha < 0.6$). For the size distribution, an increase in δT causes an increase in σ_p in the present model. For $\delta T = 24$ K the distribution width σ_p reaches a broad maximum around $f_\alpha = 0.3$, where the phase-field model indicates saturation. The reason for this difference is believed to be the geometrical difference between these two models. In the later transformation stage with severe hard impingements, the phase-field simulation allows the ferrite grains to alter their curvature to make the 'best' use of the untransformed parent structure to grow. As a result, the ferrite grains become less spherical, while they show more anisotropic growth, and thus the spread in grain size remains constant. In contrast, our present model assumes spherical growth throughout the whole transformation. The space for ferrite grains formed early in the process is limited by the continuous hard impingement, which provides the possibility for later formed ferrite grains to catch up in size. Therefore, a decrease in σ_p is observed at $\delta T = 24$ K and a weaker decrease in σ_p can be seen for $\delta T = 12$ K. Nevertheless, in general a good consistency is observed between the calculated values of δ_s and σ_p for the phase-field model and the present model.

Figure 6 shows that by simultaneously tuning δT and M_0, both models are able to replicate the experimental dilatometry data. The phase-field simulations show the best comparison for $\delta T = 0$ K and $M_0 = 2.4 \times 10^{-7}$ m^4 J^{-1} s^{-1}. Using the present model it is found that $\delta T = 0$ K, and $M_0 = 1.5 \times 10^{-7}$ m^4 J^{-1} s^{-1} show good agreement with the measurements. By increasing δT, an increase in the value of M_0 is required to achieve

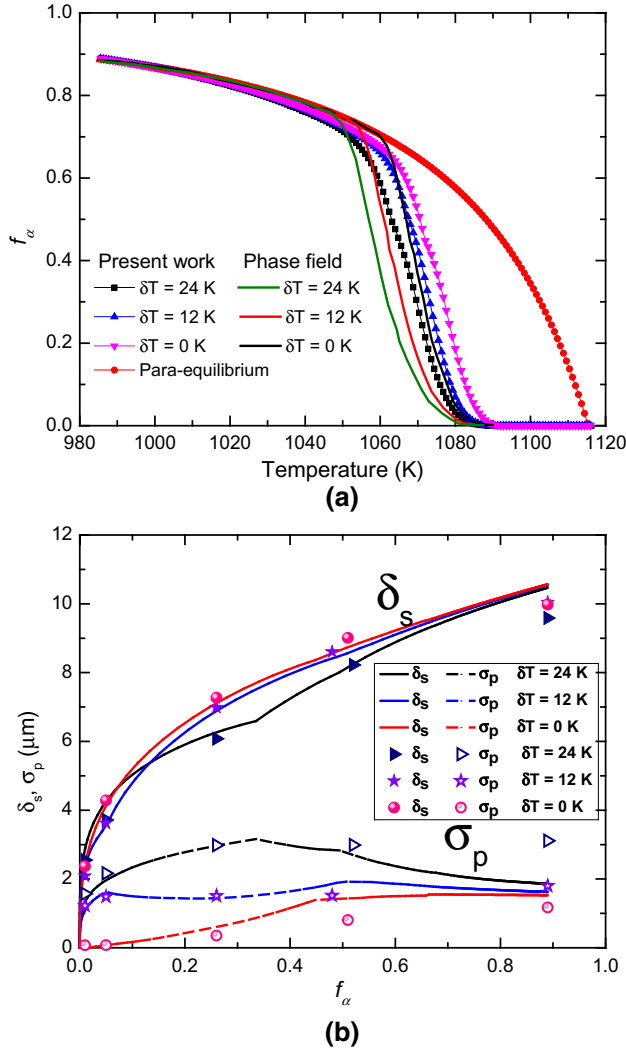Fig. 5—Effect of the nucleation temperature range δT on (a) the transformation kinetics and (b) average grain radius δ_s and the standard deviation σ_p of ferrite grain size for an interface mobility of $M_0 = 0.24 \times 10^{-6}$ m^4 J^{-1} s^{-1} at a constant cooling rate of 0.4 K/s. In (b) the phase-field simulation results are indicated by the symbols and the present modeling results correspond to the curves. The results from the phase-field model are from Mecozzi and coworkers.[20]

a good correspondence with the dilatometry data. Studying the influence of M_0 at constant δT indicates that the present model shows a smaller effective mobility than the phase-field model to achieve the same kinetics. As shown in Figure 5, both models show a comparable evolution of δ_s and σ_p as a function of f_α.

It is interesting to note that for the same time evolution of the ferrite fraction f_α during the phase transformation, the resulting ferrite grain size distribution can be distinctly different, depending on the assumptions regarding the nucleation process and the value of the interface mobility. Therefore, experimental information on the ferrite grain size distribution, as well as the ferrite fraction during the transformation will allow new insights into the nucleation and growth processes not obtainable from measurements of the ferrite fraction only.

B. Comparison Between the Simplified Nucleation Model (SNM) and the Classical Nucleation Theory (CNT)

In the previous sections, we compared the predictions for ferrite fraction and ferrite grain size (and distribution) for our present model and the earlier phase-field model, while employing the simplified nucleation model (SNM). Although SNM captures the important experimental finding that nucleation only occurs in a certain temperature range,[14] it is unrealistic to assume that the actual nucleation rate is constant over a fixed temperature window and zero outside this region. Therefore, we incorporate the nucleation rate as predicted by the CNT into our present model to investigate the difference between SNM and CNT.

Figure 7 compares the evolution of the ferrite fraction and grain size between SNM and CNT. Taking the model SNM predictions for $\delta T = 24$ K, the parameter A in the CNT model as defined in Eq. [3] is adjusted to achieve two different effects: (i) the same final ferrite grain density and (ii) the same initial ferrite nucleation rate. As shown in Figure 7(a), the predicted value of f_α for CNT with $\rho_\alpha = 2.54 \times 10^{14}$ m^{-3} overlaps with the simulation using SNM with $\delta T = 24$ K and $\rho_\alpha = 1.70 \times 10^{14}$ m^{-3}. Hence for conditions at which the nucleation rate is the same at the lowest temperature of the SNM model [1068 K (795 °C)] the same development of f_α, as well as δ_s and σ_p, is observed. Below 1068 K (795 °C), new nuclei continue to form for the CNT until ρ_α reaches a maximum value of 2.54×10^{14} m^{-3} at 1027 K (754 °C), at which stage $f_\alpha = 0.80$. During this stage, the increase in f_α in the CNT-based simulations is due to both the continuous growth of earlier formed ferrite grains and the formation of new nuclei. However, for the newly formed nuclei, the average spacing between ferrite grains is much lower, resulting in a higher chance of soft and/or hard impingement compared to that in the SNM. Therefore, the development of f_α in the CNT simulation with 2.54×10^{14} m^{-3} is comparable to the simulation with the SNM. The transformation kinetics for the CNT with $\rho_\alpha = 1.70 \times 10^{14}$ m^{-3} is considerably delayed because of the slower nucleation kinetics.

C. Carbon Diffusion and Mixed-Mode Character

As the present model is not a true 3D model, it only approximately predicts the carbon concentration in the austenite in the simulated volume. However, it contains relevant information on the interfacial carbon concentration, the effective remaining matrix carbon concentration, the diffusion length and the moment when soft and hard impingement happens for individual neighboring ferrite grains.

Figure 8 illustrates the evolution of the radial carbon diffusion profile during the austenite-to-ferrite phase transformation as a function of temperature for a selected representative ferrite grain. The spatial position of the monitored single ferrite grain is shown in the inserts of Figure 8(a). Figure 8(b) shows that up to time t_2 (at which $T \geq 1078$ K, 805 °C), the carbon diffusion field of this grain does not show overlap with
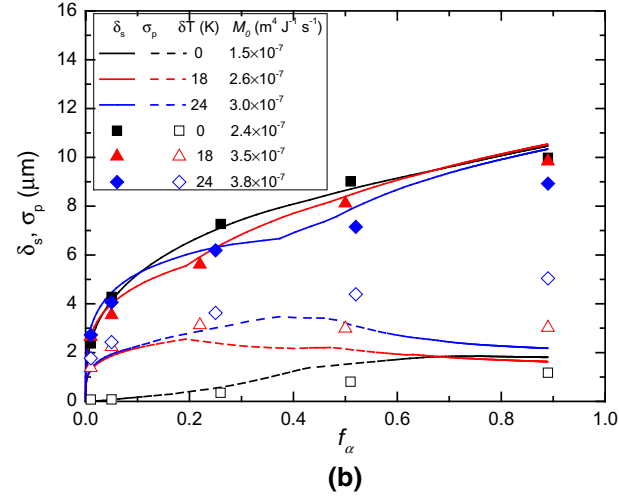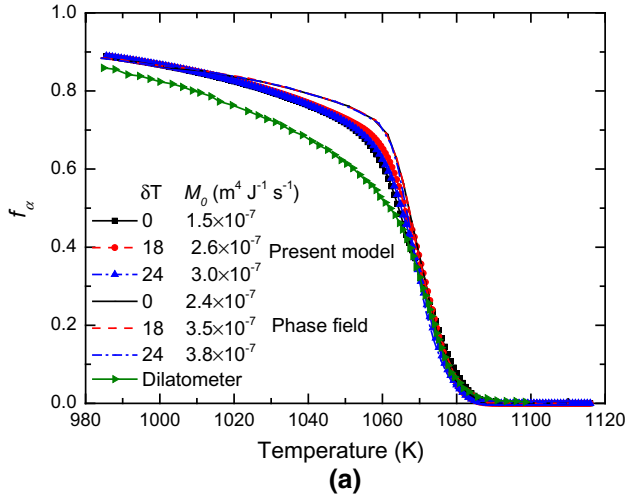
(a)

(b)

Fig. 6—Effect of nucleation temperature range δT and interface mobility M_0 on (*a*) the volume fraction of ferrite (lines are from the present model and the symbols are from the phase-field simulation[20]) and (*b*) the average grain size (lines are from the present model and the solid symbols are from the phase-field simulations[20]) and standard deviation (dashed curves are from the present model and the open symbols from the phase-field simulation[20]) at a constant cooling rate of 0.4 K/s.

surrounding diffusion fields and therefore the growth of this ferrite is not influenced by its local environment. At a time t_3 (corresponding to $T = 1069$ K, 796 °C), the carbon diffusion field for this ferrite grain starts to show overlap with the diffusion field of one of the neighboring grains, resulting in an increase of the carbon concentration in the bulk of the austenite grain. At a time t_4 ($T = 1061$ K, 788 °C), the carbon diffusion profile shows hard impingement of this ferrite grain with the nearest ferrite grain. This hard impingement leads to a dramatic increase in the interfacial carbon concentration, as shown in Figure 8(b). As a result, a pronounced transition in the grain growth velocity takes place, as indicated in Figure 8(a). As the transformation proceeds, the interfacial carbon concentration keeps increasing and finally approaches the local equilibrium concentration indicated by the dashed curve in Figure 8(b).
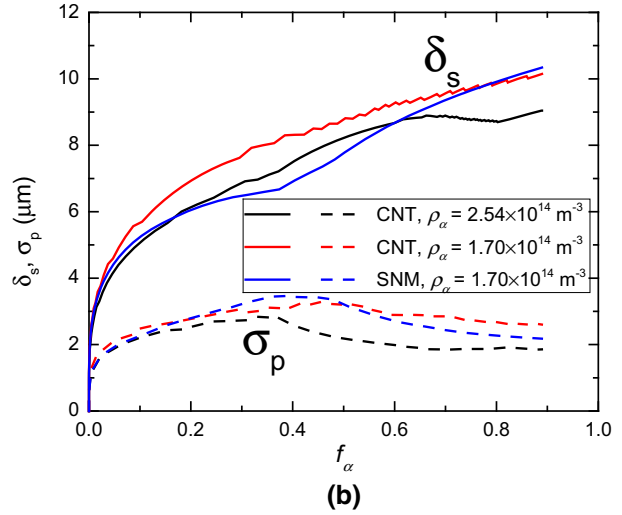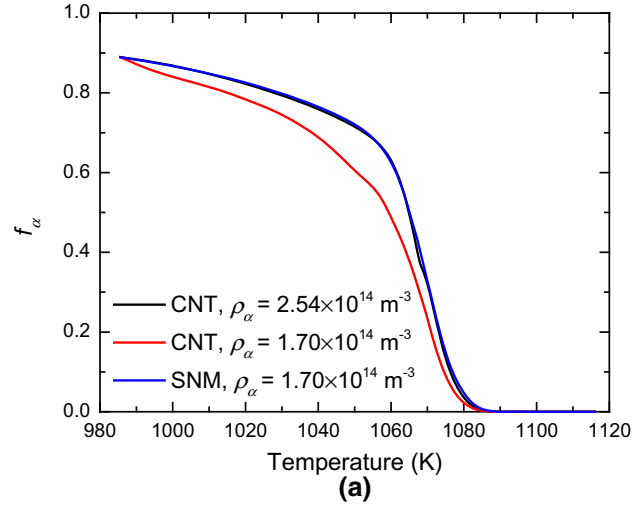

(a)

(b)

Fig. 7—Comparison of the transformation kinetics using SNM and CNT for $\delta T = 24$ K with an interface mobility of $M_0 = 3.0 \times 10^{-7}$ m^4 J^{-1} s^{-1} at a constant cooling rate of 0.4 K/s. (*a*) The volume fraction as a function of temperature and (*b*) the average grain size and standard deviation as a function of ferrite fraction.

The carbon diffusion profiles of the other ferrite grains show similar features as indicated above. All ferrite grains show an interface-controlled growth at the start of the transformation and then develop more and more into a diffusion-controlled growth until the interfacial carbon concentration approaches the equilibrium value. These detailed predictions indicate that the mixed-mode character of the moving interface is well captured in the present model, as is the case in several other mixed-mode models.[24,37,45]

IV. DISCUSSION

The model as presented here provides a computationally cheap tool to monitor the microstructural development and local carbon profiles in a realistic austenitic microstructure for a simple Fe-C-Mn steel during continuous cooling for various assumed
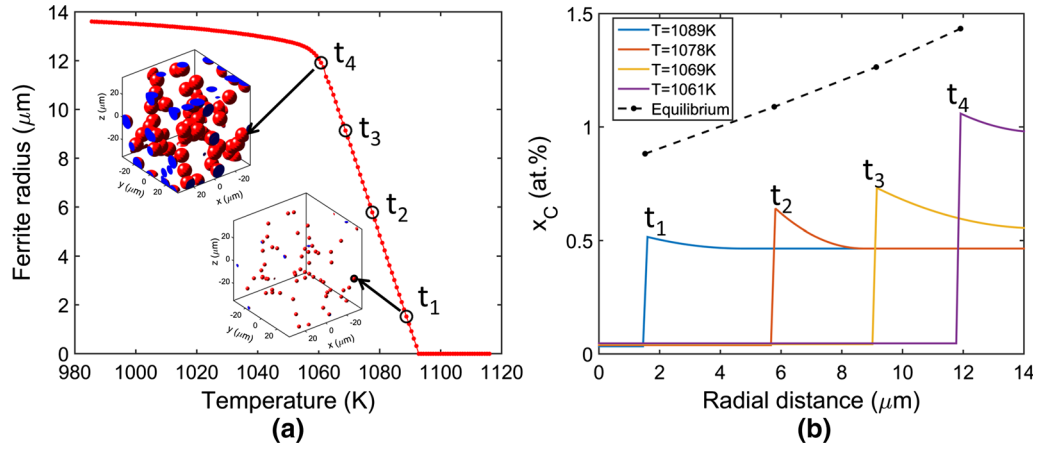
Fig. 8—Evolution of (a) a single ferrite grain radius as a function of temperature with a spatial position indicated in the inserted 3D structures and (b) diffusion profiles at four different temperatures with the times t_1, t_2, t_3, and t_4 indicated by open circles in (a). This structure is modeled with $\rho_0 = 1.7 \times 10^{14}$ m^{-3}, $\delta T = 0$ K, and $M_0 = 1.5 \times 10^{-7}$ m^4 J^{-1} s^{-1} at a constant cooling rate of 0.4 K/s.
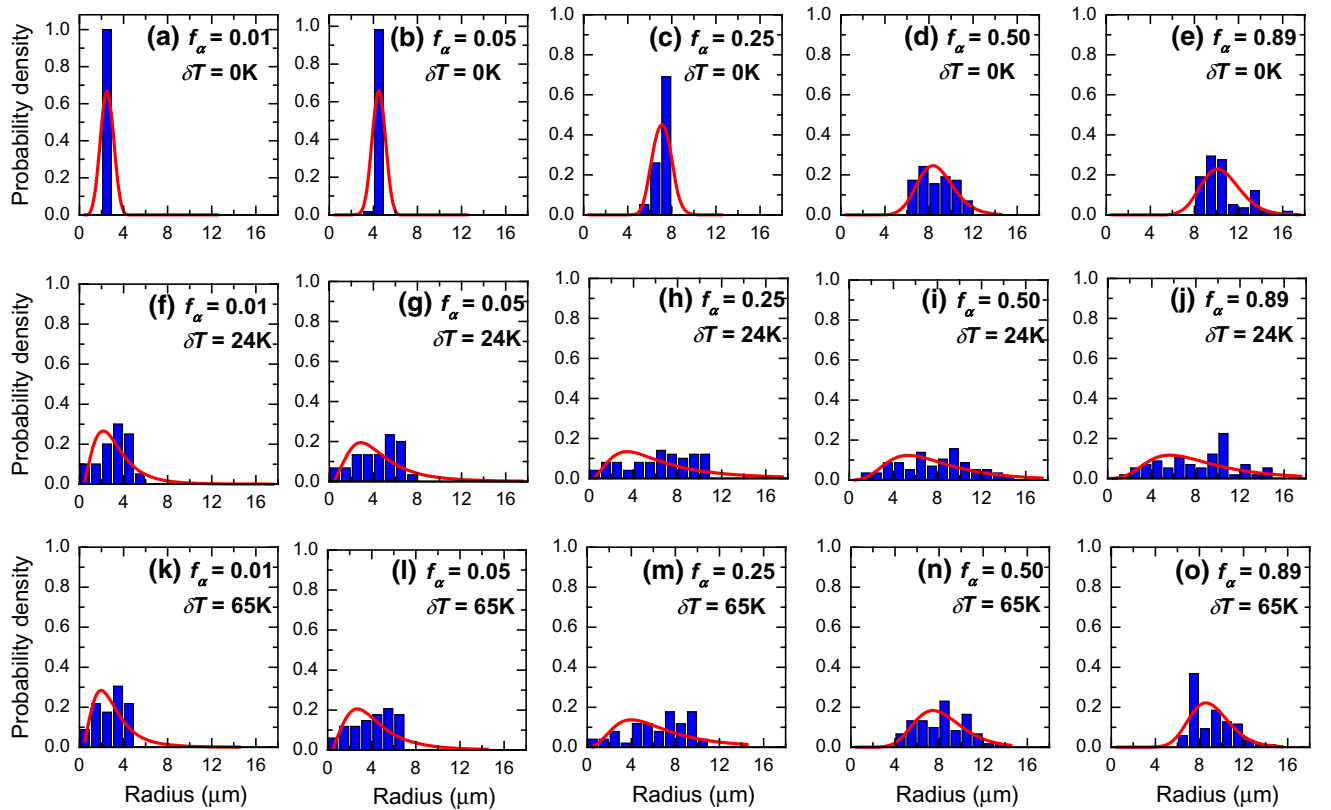

Fig. 9—Effect of the nucleation temperature range δT on the grain size distribution at a ferrite phase fraction of $f_\alpha = 0.01$, 0.05, 0.25, 0.50, and 0.89, respectively. (a) through (e) is modeled with $\rho_0 = 1.7 \times 10^{14}$ m^{-3}, $\delta T = 0$ K, and $M_0 = 1.5 \times 10^{-7}$ m^4 J^{-1} s^{-1}; (f) through (j) is modeled with $\rho_0 = 1.7 \times 10^{14}$ m^{-3}, $\delta T = 24$ K, and $M_0 = 3.0 \times 10^{-7}$ m^4 J^{-1} s^{-1} using SNM; and (k) through (o) is modeled with $\rho_0 = 2.5 \times 10^{14}$ m^{-3}, $\delta T = 65$ K, and $M_0 = 3.0 \times 10^{-7}$ m^4 J^{-1} s^{-1} using CNT. Lognormal fits are shown in solid curves. All simulations show the name transformation kinetics as the dilatometer measurement for a constant cooling rate of 0.4 K/s.

nucleation conditions. The ferrite grain size distribution is a crucial output parameter of this model. Although experimental information on the grain size distribution has traditionally been restricted to destructive techniques (imaging analysis on quenched samples), recent advances in radiation techniques like micro-beam synchrotron X-ray diffraction[14,15] and neutron depolarization[17,18] can provide *in-situ* time-resolved information on the ferrite grain size during the transformation. The present model may bridge (at relatively limited computationally efforts) the gap between the experimental ferrite fraction, ferrite grain density, average ferrite grain size and the ferrite grain size distribution, and its metal physical interpretation in key microstructural processes. Below, the time evolution of the ferrite grain size distribution at an identical overall

Table II. The Mean (E) and Standard Deviation (SD) of the Effective Ferrite Grain Size Distribution Derived from Lognormal Fits to the Modeling Results in Three Different Conditions

f_α	$\delta T = 0$ K, SNM		$\delta T = 24$ K, SNM		$\delta T = 65$ K, CNT	
	E (μm)	SD (μm)	E (μm)	SD (μm)	E (μm)	SD (μm)
0.01	2.4 (1)	0.0007 (3)	3.2 (9)	2.0 (9)	2.9 (8)	1.9 (8)
0.05	4.2 (1)	0.07 (2)	4.6 (8)	3.0 (9)	4.3 (9)	2.9 (7)
0.25	7.1 (2)	0.6 (2)	6.7 (9)	5.4 (9)	6.7 (9)	4.5 (6)
0.50	8.7 (5)	1.6 (4)	8.0 (4)	4.5 (8)	8.3 (9)	2.3 (5)
0.89	10.5 (5)	1.7 (5)	8.4 (8)	4.8 (6)	9.0 (5)	1.8 (4)

ferrite fraction evolution is elaborated in more detail, in order to demonstrate the added-value of this new transformation model.

In Figure 9, the ferrite grain size distribution is shown at specific transformation levels f_α, for three assumed simulations. Although these simulations show the same transformation kinetics (measurable in conventional experiments such as dilatometry), obtained by adjusting the interface mobility value and nucleation rate, significant differences in the evolution of the ferrite size distribution are observed. For an SNM simulation with $\delta T = 0$ K, the width of the size distribution is relatively small, although it increases with increasing f_α due to the increased occurrence of hard impingement. For an SNM simulation with $\delta T = 24$ K or a CNT simulation with $\delta T = 65$ K, the size distributions are comparable but only up to a transformation fraction of $f_\alpha = 0.05$. For higher ferrite fractions the size distribution for $\delta T = 24$ K with SNM shows a wider grain size distribution. This is due to hard impingement to set in later in the SNM simulation than for the case for the CNT simulation with $\delta T = 65$ K.

Based on the above results, it is clear that the ferrite grain size distribution is a valuable link to the system characteristics δT and M_0. The solid curves in Figure 9 present the fittings of the simulated data to a lognormal grain size distribution:

$$F(R_\alpha | \mu, \sigma) = \frac{1}{R_\alpha \sigma \sqrt{2\pi}} \exp\left[-\frac{(\ln R_\alpha - \mu)^2}{2\sigma^2}\right], \quad [33]$$

where R_α is the effective ferrite grain radius and μ and σ are the parameters of the lognormal distribution. For the lognormal distribution the mean corresponds to $E = \exp(\mu + \sigma^2/2)$ and the variance VAR = $SD^2 = \exp(2\mu + \sigma^2)[\exp(\sigma^2) - 1]$, with the standard deviation SD. The derived parameters from the fits are given in Table II. For $\delta T = 0$ K the average ferrite grain radius E differs significantly from the other two nucleation modes, especially at the later transformation stages. This difference is less pronounced in the standard deviation of the ferrite grain radius SD. The fitting parameters for $\delta T = 24$ K with SNM and $\delta T = 65$ K with CNT are in close agreement with each other for $f_\alpha < 0.25$ and only start to show differences for higher ferrite fractions.

The above analysis suggests that from experimentally determined values for both the ferrite fraction and the average grain size at a particular stage of the transformation, it is possible to derive accurate estimates for the underlying physical parameters δT and M_0. However, given the E and SD values, there are multiple solutions for specific combinations of δT, M_0, and nucleation to describe the ferrite grain size distribution for one specific f_α level. Only by analyzing the ferritic grain size data for different f_α levels it is possible to derive accurate estimates of the key physical parameters.

V. CONCLUSIONS

A 3D model that couples classical nucleation theory and the interface moving under mixed-mode interface condition has been developed for ferrite formation in Fe-C-Mn steels during continuous cooling. This model predicts a comparable transformation kinetics as a published phase-field model and matches the experimental dilatometric data for linear cooling of an Fe-0.10C-0.49Mn (wt pct) steel. The influence of the increased nucleation temperature range on the γ-α transformation kinetics can be counteracted by increasing interface mobility. However, the evolution of the ferrite grain size distribution would be distinctly different, which cannot be undone by tuning the modeling parameters. A comparison between the simplified nucleation model and the classical nucleation theory shows that a close similarity in nucleation behavior in the early stage results in a similar evolution of ferrite fraction for the entire transformation process. Analyzing grain size distribution for different f_α levels is required to derive accurate estimates of the key physical parameters, the nucleation temperature interval, and the effective interface mobility for the γ-α phase transformation in this C-Mn steel.

priate credit to the original author(s) and the source, provide a link to the Creative Commons license, and indicate if changes were made.

REFERENCES

1. W. Bleck: *JOM*, 1996, vol. 48, pp. 26–30.
2. D.V. Edmonds, K. He, F.C. Rizzo, B.C. De Cooman, D.K. Matlock, and J.G. Speer: *Mater. Sci. Eng. A*, 2006, vol. 438, pp. 25–34.
3. S. Winkler, A. Thompson, C. Salisbury, M. Worswick, I. Van Riemsdijk, and R. Mayer: *Metall. Mater. Trans. A*, 2008, vol. 39A, pp. 1350–58.
4. O. Bouaziz, H. Zurob, and M. Huang: *Steel Res. Int.*, 2013, vol. 84, pp. 937–47.
5. H.S. Zurob, C.R. Hutchinson, Y. Brechét, H. Seyedrezai, and G.R. Purdy: *Acta Mater.*, 2009, vol. 57, pp. 2781–92.
6. X. Zhong, D.J. Rowenhorst, H. Beladi, and G.S. Rohrer: *Acta Mater.*, 2017, vol. 123, pp. 136–45.
7. E. Novillo, D. Hernández, I. Gutiérrez, and B. López: *Mater. Sci. Eng. A*, 2004, vol. 385, pp. 83–90.
8. A. Phillion, H.W. Zurob, C.R. Hutchinson, H. Guo, D.V. Malakhov, J. Nakano, and G.R. Purdy: *Metall. Mater. Trans. A*, 2004, vol. 35A, pp. 1237–42.
9. F. Barbe and R. Quey: *Int. J. Plast.*, 2011, vol. 27, pp. 823–40.
10. E.A. Jägle and E.J. Mittemeijer: *Acta Mater.*, 2011, vol. 59, pp. 5775–86.
11. B. Zhu, Y. Zhang, C. Wang, P.X. Liu, W.K. Liang, and J. Li: *Metall. Mater. Trans. A*, 2014, vol. 45A, pp. 3161–71.
12. G. Purdy, J. Ågren, A. Borgenstam, Y. Bréchet, M. Enomoto, E. Gamsjager, M. Gouné, M. Hillert, C. Hutchinson, M. Militzer, and H. Zurob: *Metall. Mater. Trans. A*, 2011, vol. 42A, pp. 3703–18.
13. M. Gouné, F. Danoix, J. Ågren, Y. Bréchet, C.R. Hutchinson, M. Militzer, G. Purdy, S. van der Zwaag, and H. Zurob: *Mater. Sci. Eng. R*, 2015, vol. 92, pp. 1–38.
14. S.E. Offerman, N.H. van Dijk, J. Sietsma, S. Grigull, E.M. Lauridsen, L. Margulies, H.F. Poulsen, M.Th. Rekveldt, and S. van der Zwaag: *Science*, 2002, vol. 298, pp. 1003–05.
15. M. Militzer: *Science*, 2002, vol. 298, pp. 975–76.
16. S.G.E. te Velthuis, N.H. van Dijk, M.Th. Rekveldt, J. Sietsma, and S. van der Zwaag: *Acta Mater.*, 2000, vol. 48, pp. 1105–14.
17. S.E. Offerman, L.J.G.W. van Wilderen, N.H. van Dijk, M.Th. Rekveldt, J. Sietsma, and S. van der Zwaag: *Acta Mater.*, 2003, vol. 51, pp. 3927–38.
18. S.G.E. te Velthuis, N.H. van Dijk, M.Th. Rekveldt, J. Sietsma, and S. van der Zwaag: *Mater. Sci. Eng. A*, 2000, vol. 277, pp. 218–28.
19. S.E. Offerman, N.H. van Dijk, J. Sietsma, E.M. Lauridsen, L. Margulies, S. Grigull, H.F. Poulsen, and S. van der Zwaag: *Acta Mater.*, 2004, vol. 52, pp. 4757–66.
20. M.G. Mecozzi, M. Militzer, J. Sietsma, and S. van der Zwaag: *Metall. Mater. Trans. A*, 2008, vol. 39A, pp. 1237–47.
21. K.F. Kelton: in *Solid State Physics*, H. Ehrenreich and D. Turnbull, eds., Academic Press, New York, NY, 1991, vol. 45, p. 75.
22. D. Kashchiev: *Nucleation, Basic Theory with Applications*, Butterworth-Heinemann, Oxford, OX, 2000, pp. 184–270.
23. H.I. Aaronson, M. Enomoto, and J.K. Lee: *Mechanisms of Diffusional Phase Transformations in Metals and Alloys*, CRC Press, Boca Raton, 2010, pp. 49–245.
24. J. Sietsma and S. van der Zwaag: *Acta Mater.*, 2004, vol. 52, pp. 4143–52.
25. W. Huang and M. Hillert: *Metall. Mater. Trans. A*, 1996, vol. 27A, pp. 480–83.
26. M. Herceg, M. Kvasnica, C.N. Jones, and M. Morari: Proc. of the European Control Conference, Zurich, Switzerland, July 17–19, 2013, pp. 502–10, http://control.ee.ethz.ch/~mpt.
27. N.H. van Dijk, S.E. Offerman, J. Sietsma, and S. van der Zwaag: *Acta Mater.*, 2007, vol. 55, pp. 4489–98.
28. H. Song and J.J. Hoyt: *Phys. Rev. Lett.*, 2016, vol. 117, p. 238001-05.
29. H. Sharma, J. Sietsma, and S.E. Offerman: *Sci. Rep.*, 2016, vol. 6, p. 30860.
30. K.M. Lee, H.C. Lee, and J.K. Lee: *Philos. Mag.*, 2010, vol. 90, pp. 437–59.
31. G.P. Krielaart, J. Sietsma, and S. van der Zwaag: *Mater. Sci. Eng. A*, 1997, vol. 237, pp. 216–23.
32. M. Hillert and B. Sundman: *Acta Metall.*, 1976, vol. 24, pp. 731–43.
33. H. Buken and E. Kozeschnik: *Metall. Mater. Trans. A*, 2017, vol. 48A, pp. 2812–18.
34. E. Gamsjäger, M. Wiessner, S. Schider, H. Chen, and S. van der Zwaag: *Philos. Mag.*, 2015, vol. 95, pp. 2899–917.
35. H. Chen and S. van der Zwaag: *J. Mater. Sci.*, 2011, vol. 46, pp. 1328–36.
36. J. Ågren: *Scripta Metall.*, 1986, vol. 20, pp. 1507–10.
37. C. Bos and J. Sietsma: *Scripta Mater.*, 2007, vol. 57, pp. 1085–88.
38. K.D. Gibson and H.A. Scheraga: *J. Phys. Chem.*, 1987, vol. 91, pp. 4121–22.
39. E.J. Mittemeijer and F. Sommer: *Z. Metallkd.*, 2002, vol. 93, pp. 352–61.
40. M. Hillert and L. Höglund: *Scripta Mater.*, 2006, vol. 54, pp. 1259–63.
41. J. Zhu, H. Luo, Z. Yang, C. Zhang, S. van der Zwaag, and H. Chen: *Acta Mater.*, 2017, vol. 133, pp. 258–68.
42. M. Militzer, M.G. Mecozzi, J. Sietsma, and S. van der Zwaag: *Acta Mater.*, 2006, vol. 54, pp. 3961–72.
43. I. Steinbach, F. Pezzolla, B. Nestler, M. Seeßelberg, R. Prieler, G.J. Schmitz, and J.L.L. Rezende: *Phys. D Nonlinear Phenom.*, 1996, vol. 94, pp. 135–47.
44. L.Q. Chen: *Annu. Rev. Mater. Res.*, 2002, vol. 32, pp. 113–40.
45. C. Bos and J. Sietsma: *Acta Mater.*, 2009, vol. 57, pp. 136–44.